This article has been accepted for inclusion in a future issue of this journal. Content is final as presented, with the exception of pagination.

A Multi-Degradation Aided Method for Unsupervised Remote Sensing Image Super Resolution With Convolution Neural Networks

Ning Zhang, Yongcheng Wang, Xin Zhang, Dongdong Xu, Xiaodong Wang, Guangli Ben, Zhikang Zhao, and Zheng Li

***Abstract*— In remote sensing, it is desirable to improve image resolution by using the image super-resolution (SR) technique. However, there are two challenges: the first one is that high-resolution (HR) images are insufficient or unavailable; another one is that the single degradation model such as bicubic (BIC) cannot super-resolve favorable images in the real world. To address the above two problems, this article presents a multi-degradation, unsupervised SR method based on deep learning. This framework consists of a degrader *D* to fit the image degradation model and a generator *G* to generate SR image. By introducing *D*, calculating the loss function between SR image and HR image as supervised SR methods did can be converted into calculating loss between low resolution (LR) image and image degraded by SR image, thereby realizing unsupervised learning. Experiments on several degradation models show that our method renders the state-of-the-art results compared with existing unsupervised SR methods, and achieves competitive results in contrast with supervised SR methods. Moreover, for real remote sensing images obtained by the Jilin-1 satellite, our method obtained more plausible results visually, which demonstrate the potential in real-world applications.**

***Index Terms*— Deep neural network (DNN), multi-degradation, remote sensing image, super-resolution (SR), unsupervised learning.**

I. Introduction

HIGH resolution remote sensing images have a wide range of applications, such as environmental monitoring [1], object detection [2], and resource exploration [3]. However, the acquisition of high-resolution (HR) remote sensing images requires high precision imaging equipment and ideal data production conditions, and we never have access to any real HR remote sensing images other than a single low resolution (LR) image. Super-resolution (SR) technology can effectively improve image resolution through image processing techniques without improving existing imaging equipment. Given the reasons that the high cost of improving imaging equipment and the restriction of the imaging system, it is of great significance to research on remotely sensed image SR.

Deep learning (DL) has developed rapidly in image processing. And these years have seen an upsurge of using DL models for single image super resolution (SISR) since they achieved the state-of-the-art results. But current DL-based methods of remote sensing image SR still require further study, considering the following problems.

First of all, the current SISR methods based on DL typically rely on HR images as references. For natural images, some supervised SR methods [4]–[7] have obtained the ideal results. But as mentioned before, it is difficult to obtain HR remote sensing images in the real world. In this case, it is necessary to construct unsupervised SR methods without using HR images as labels.

Second, SR is one of the classical ill-posed inverse problems in low-level computer vision, because there are infinitely many HR images that could be degraded to the same one LR image. The general degradation model of remote sensing images is formulated as (1)

$$I^{\mathrm{LR}} = (I^{\mathrm{HR}} \otimes k) \downarrow_r + n \tag{1}$$

where I^{HR} represents real HR images, k denotes blur kernels, $\downarrow_r$ is a downsampling operation with scale factor r, and n is typically additive white Gaussian noise (AWGN) with standard deviation σ (noise level). Existing DL-based methods mostly adopted simplified degradation, such as bicubic (BIC) degradation. However, the effectiveness of these methods is very limited in practical use due to the inconsistency between the simplistic degradation assumption of existing SISR methods and the complex degradations of real images, which indicates the necessity of taking multiple degradation models into consideration in SR. The closer the degradation model to that of real images, the better SR results can be obtained when multi-degradation is included to generate synthetic LR images. Kai [8] took degradation model into consideration and introduced a dimensionality stretching strategy which

Manuscript received November 24, 2020; accepted November 27, 2020. This work was supported by the Chinese Academy of Sciences. *(Corresponding author: Yongcheng Wang.)*

Ning Zhang, Xin Zhang, Guangli Ben, Zhikang Zhao, and Zheng Li are with the Changchun Institute of Optics, Fine Mechanics and Physics, Chinese Academy of Sciences, Changchun 130033, China, and also with the School of Optoelectronics, University of Chinese Academy of Sciences, Beijing 100049, China (e-mail: zhangning171@mails.ucas.ac.cn; zhangxin162@mails.ucas.ac.cn; benguangli@ciomp.ac.cn; zhaozhikang20@mails.ucas.ac.cn; lizheng20@mails.ucas.ac.cn).

Yongcheng Wang, Dongdong Xu, and Xiaodong Wang are with the Changchun Institute of Optics, Fine Mechanics and Physics, Chinese Academy of Sciences, Changchun 130033, China (e-mail: wangyc@ciomp.ac.cn; xudongdong@ciomp.ac.cn; wangxd@ciomp.ac.cn).

Color versions of one or more figures in this article are available at https://doi.org/10.1109/TGRS.2020.3042460.

Digital Object Identifier 10.1109/TGRS.2020.3042460

0196-2892 © 2020 IEEE. Personal use is permitted, but republication/redistribution requires IEEE permission.
See https://www.ieee.org/publications/rights/index.html for more information.

Authorized licensed use limited to: Changchun Inst of Optics Fine Mechanics & Physics. Downloaded on April 19,2021 at 02:22:52 UTC from IEEE Xplore. Restrictions apply.

This article has been accepted for inclusion in a future issue of this journal. Content is final as presented, with the exception of pagination.

facilitated the deep neural network (DNN) to handle multiple degradations involved blur kernels and noise. And this strategy helps extend current DL-based SR methods from BIC degradation to the new degradation models and exploit the power of DNNs.

Finally, DL-based SR methods typically utilize the information of a large number of image data sets and the corresponding relationship between LR and HR images. But most of them make little use of the internal image prior such as the self-similarity and sparsity prior. Lempitsky *et al.* [9] had pointed out that the prior imposed by DNNs that researched in their work is highly related to self-similarity and dictionary-based priors. Hence, the priors of one single image can be introduced by using the framework in [9].

Given the problems and related works above, we propose a convolutional neural network (CNN)-based unsupervised SR method constructed by an image generator G and a degrader D. First, the degrader is trained by a large synthetic image data set to fit the multi-degradation models of real images, which can also introduce external prior information of remote sensing images. And then we followed [9], using a plug-and-play framework to investigate the prior of one single image. Our method introduced the trained degrader D to degrade the super-resolved image I^{SR} obtained by generator G into LR-sized image $I^{\mathrm{SR}'}$, and minimized the loss between $I^{\mathrm{SR}'}$ and LR image I^{LR} to realize unsupervised learning. The details of our proposed method are introduced in Section III.

The main contributions of this work are as follows:

1) A CNN D is proposed to simulate the multiple degradation models of real remote sensing images. This degrader is able to introduce external prior information of data sets and the multi-degradation information when degrading the reconstructed images and calculate the loss between $I^{\mathrm{SR}'}$ and I^{LR}, thereby achieving the purpose of unsupervised SR.
2) The generative network G accepts a single image as input to exploit the internal image prior, and is restrained by the degrader and loss function, which can make full use of image priors and external image information.
3) G and D constitute the proposed unsupervised SR method. The experimental results show competitive performance compared with several supervised SR methods and the state-of-the-art results of unsupervised SR methods. Besides, our method achieves satisfactory performance in real remote sensing images.

The rest parts of this article are as follows: Section II describes the related works on the development of SR, including supervised and unsupervised learning models. Section III presents an overview of the proposed method and the details of network structures G and D. Section IV describes the implementation and experimental results on both synthetic images and real images with an analysis. Finally, conclusions are provided in Section V.

II. Related Works

A. Background of Image SR

Image super-resolution algorithms are usually classified into interpolation-based, reconstruction-based, and learning-based methods. Among them, interpolation-based algorithms include the nearest, BIC and Lanczos [10]. And these algorithms are generally used to preprocess images for the subsequent reconstruction-based or learning-based SR methods. Reconstruction-based algorithms exploit priors within an image and build image models to restrain the SR process of images. Representative algorithms are iterative back-projection (IBP) [11], deconvolution [12]–[14], and regularization [15], [16]. Learning-based methods utilize external or internal information to recover the desired details in HR images. Over the decades, learning-based methods has covered popular algorithms involved in sparse coding [17]–[19], machine learning [20]–[22], and DL. Since Chao [4] first introduced CNN into SR, massive SR methods based on DL have appeared. Methods such as EDSR [5], SRGAN [6], RCAN [7] were proposed successively. With the situation that RCAN achieved the best result in BIC degradation but still had difficulty in super-resolving real images, researchers began to focus on multiple degradation models. SRMD introduced a dimensionality stretching strategy to integrate noise and blur into training. And DPSR [23], UDVD [24], and USRNet [25] then followed SRMD in multi-degradation models and updated the SR results gradually.

In many application scenarios, SR methods based on DL have achieved state-of-the-art results, and one of the most significant applications is in remote sensing. In DL-based methods, the primary strategy was using transfer learning to handle the insufficiency of HR data. Ducournau and Fablet [26] and Ma *et al.* [27] fine-tuned the existing models like SRCNN and GAN [28] to super-resolved remotely sensed images. Lei *et al.* [29] proposed a local–global combined network for remote sensing image SR. Pan *et al.* [30] utilized residual learning and backprojection block to improve the resolution of remotely sensed images with median and even large ratio. Ma *et al.* [31] incorporated a recursive ResNet and the wavelet transform in the frequency domain to realize remote sensing image SR. Lei *et al.* [32] introduced a coupled-discriminated GAN to address the "discrimination-ambiguity" and improve the quality of SR images. Andrea *et al.* [33] proposed a CNN-based technique that exploits both spatial and temporal correlations to combine multiple images for multiframe image SR. Zhang *et al.* [34] proposed a multiscale attention network to extract the multilevel features and a scene-adaptive SR strategy for remote sensing image SR. In hyperspectral remote sensing images, it is important to improve special resolution but keep the spectral fidelity. Yi *et al.* [35] proposed a hyperspectral-multispectral fusion method for hyperspectral image SR with spatial and spectral correlations and proper regularization. Xie *et al.* [36] proposed a deep feature matrix factorization model with DNN to super-resolved hyperspectral images while preserving better spectral information. Fotiadou *et al.* [37] introduced a postacquisition computational technique to enhance the spectral resolution by exploiting the mathematical frameworks of sparse representations and dictionary learning for hyperspectral image unmixing. Arun *et al.* [38] proposed the design of 3-D-CNN-based SISR architectures that can map the spatial-spectral characteristics of hyperspectral images to a finer spatial resolution using

Authorized licensed use limited to: Changchun Inst of Optics Fine Mechanics & Physics. Downloaded on April 19,2021 at 02:22:52 UTC from IEEE Xplore. Restrictions apply.

This article has been accepted for inclusion in a future issue of this journal. Content is final as presented, with the exception of pagination.

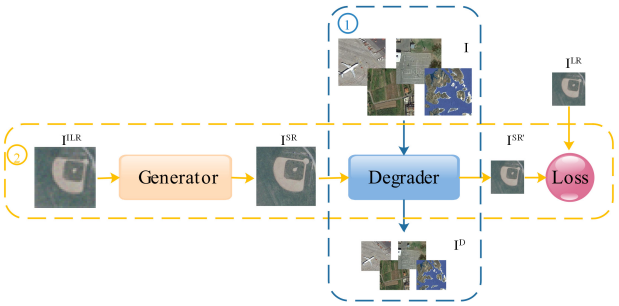

Fig. 1. Overview of the proposed unsupervised SR method.

simultaneous optimization of sparse codes and dictionaries. The above all SR methods utilize the available resolution remote sensing images as HR images for supervised image SR.

B. Unsupervised Image SR

Goodfellow *et al.* [39] had pointed out that unsupervised learning and supervised learning are not formally defined terms since the lines between them are often blurred. Unsupervised learning in SR can be informally defined by not using HR images for reconstruction. There are several classical unsupervised SR methods before the rise of DL such as the example-based method [20]–[22] and blind SR method [40]. The first unsupervised SR model based on DNNs is "Zero-Shot" SR (ZSSR) [41]. ZSSR exploited the internal recurrent information within a single image and then super-resolved this image. Zhao *et al.* [42] trained bidirectional cyclic network with the degradation and reconstruction process using data sets of different resolutions. Yuan *et al.* [43] designed a Cycle-in-Cycle GAN without using images in pairs, thereby making it an unsupervised SR method. In remote sensing, several unsupervised methods were proposed since the unavailable characteristic of HR images. Haut *et al.* [44] avoided using HR images by adopting the Lanczos kernel as a downsampler. Zhang *et al.* [45] downsampled SR images with pooling layers in a GAN framework to super-resolve images with available resolution images. Hou and Zhang [46] proposed a reverse generating network and an adaptive domain distance measurement network for unsupervised learning SR. Wang *et al.* [47] followed [43], and trained two generative networks as a cycle using unpaired remote sensing images.

III. Method

The energy function of the maximum a posteriori estimation (MAP) framework is shown in (2)

$$\min_{x} \|y - (x \otimes k) \downarrow\|^2 + \beta\Phi(x) \tag{2}$$

where x and y represent HR image and LR image in image SR, respectively. k denotes blur kernels, $\downarrow$ is a downsampling operation, and β is a balanced coefficient. Therefore, the HR image could be estimated by the data fidelity term $\|y - (x \otimes k) \downarrow\|$, which corresponds to the image degradation model, and regularization term (or prior term) $\Phi(x)$. Fig. 1 illustrates the overall structure of the proposed method. According to the MAP framework, this work utilizes the degrader network D to fit the degradation model and extracts external information from data sets. D consists of modules of cascaded convolutional, rectified linear unit (ReLU), and batch normalization (BN) layers with residual learning. And the generative network G exploits the internal prior information within a single image, which contains a series of downsample and upsample blocks with skip connections, and these skip connections also consist of convolutional, BN, and Leaky ReLU layers. Once the degrader is trained, G together with the degrader D forms a plug-and-play unsupervised SR method and they explore the prior information and degradation information in one framework.

In Fig. 1, first, the degradation network D is trained by a large synthesized remote sensing image data set. And then, an image I^{ILR} interpolated by BIC is fed into the generative network, obtaining an SR image I^{SR}. Typically in supervised SR methods, SR image I^{SR} is going to compute loss function with HR image I^{HR}, as illustrated in (3)

$$\min \ \mathrm{Loss}(I^{\mathrm{SR}}, I^{\mathrm{HR}}). \tag{3}$$

However, there is no HR label in unsupervised SR. Therefore, the SR image I^{SR} is degraded by the degradation network D, and the loss function is transferred into computing loss between degraded image $I^{\mathrm{SR}'}$ and LR image I^{LR}, as is shown in (4)

$$\min \ \mathrm{Loss}(I^{\mathrm{SR}}, I^{\mathrm{HR}}) \rightarrow \min \ \mathrm{Loss}(I^{\mathrm{SR}'}, I^{\mathrm{LR}}). \tag{4}$$

The proposed method does not require HR images. More details on D, G and loss function are provided next.

A. Degradation Network D

According to (1), the degrader D has to fit the image degradation model as blurring, downsampling, and adding noises. To train D, we adopt the strategy as [8], where anisotropic Gaussian blur kernels, BIC downsampling, and AWGN are used to synthesize image data set, but there are some changes about parameter settings (seeing Section IV-A). And the blur kernels and noise are also stretched to 2-D feature and concatenated with degraded image, so the synthesized images have 19 channels.

The proposed D network for multiple degradations is illustrated in Fig. 2. D takes 3-channel images with a size of $H \times W$ as input and output 19-channel images and features with a size of $(H/r) \times (W/r)$, where r denotes ratio (or scale factor). The 19 channels of output include the 3-channel downsampled image, the 15-channel blur kernel features, and the 1-channel noise feature of multi-degradation. The main structures in D are cascaded convolutional layers, ReLU, and BN with residual learning. And the downsampling operation is achieved by convolutional layers with a stride of 2. Before the stride convolutional layer, there are long-term skip connections to preserve as more information on large-size images and features as possible.

B. Generative Network G

Once the D is determined, the next operation is to construct the SR framework. Followed [9], we adopt the "skip" network as our generative network G. In Fig. 3, a BIC interpolated

Authorized licensed use limited to: Changchun Inst of Optics Fine Mechanics & Physics. Downloaded on April 19,2021 at 02:22:52 UTC from IEEE Xplore. Restrictions apply.

This article has been accepted for inclusion in a future issue of this journal. Content is final as presented, with the exception of pagination.

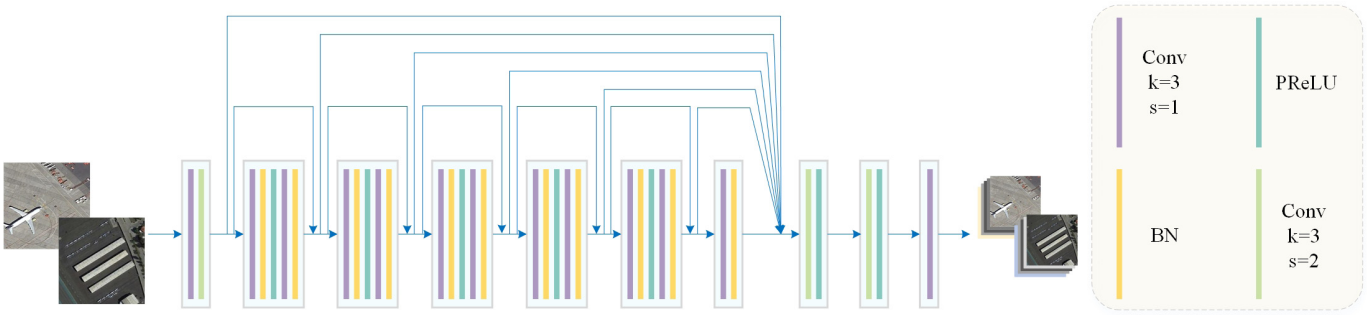

Fig. 2. Structure of the degrader D. It consists of modules of cascaded convolutional, ReLU and BN layers with residual learning.

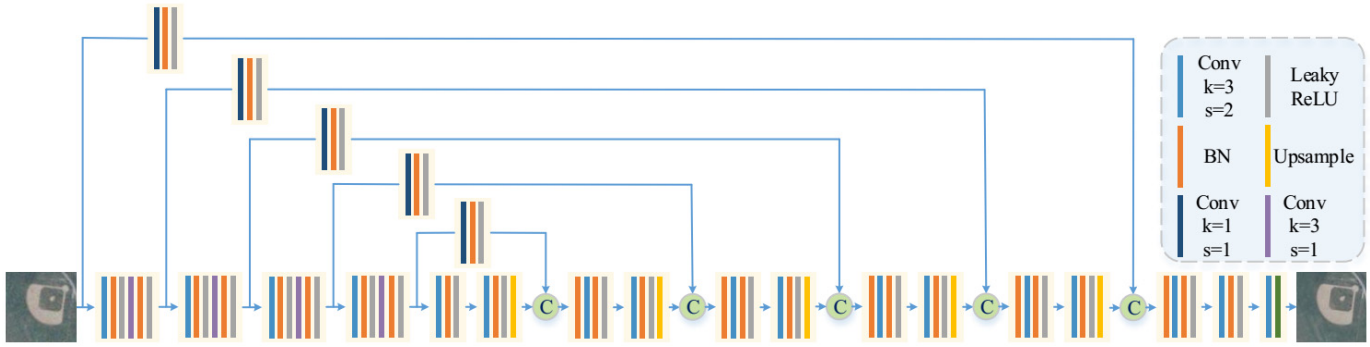

Fig. 3. Structure of the generator G. It contains a series of downsample and upsample blocks with skip connections, and these skip connections are also consist of convolutional, BN, and Leaky ReLU layers.

image with blur kernels and noise features is fed into G, and after a series of downsampling and upsampling with skip connections, a 3-channel SR image is obtained. But there are no HR images to help train G. Therefore, G has to wait until the SR image is fed into D and calculate the loss function to update the parameter.

C. Loss Function

As mentioned before, the proposed method does not require HR images because it degrades the super-resolved image and adopts designed loss functions. The loss functions of D and G are designed for a different purpose.

The primary task of D is to generate degraded images, and in the meantime, D has to learn the degradation information. In this work, the degradation information is represented by the blur kernel and noise maps. So the loss function of D has two components, and we set a coefficient ω to balance the loss, as illustrated in (5)

$$\text{Loss}_D = L_2(I^D, I^{\text{LR}_0}) + \omega \times L_2(F^D, F^{\text{LR}_0}) \tag{5}$$

where I^{LR_0} represent the synthetic LR image, and I^D is the degraded LR image (3-channel output of D), F^{LR_0}, and F^D are the default degradation maps and estimated degradation maps (the other 16-channel output of D), respectively. And ω was set to 0.5 in our experiments.

For G, the loss function has to wait until the SR image is fed into D and calculated as (6)

$$\text{Loss}_G = L_2(I^{\text{SR}'}, I^{\text{LR}}) \tag{6}$$

where I^{LR} and $I^{\text{SR}'}$ represent the LR image and degraded SR image. This time we prefer to make $I^{\text{SR}'}$ approximate I^{LR} to update the parameter of G, so the degradation feature maps are not included in the loss.

IV. Experiment

A. Data Set and Implementation Details

The experiments of training D were performed on two widely used benchmark data sets in remote sensing, UC Merced data set [48] and NWPURESIS45 [49], where 70% for training and 30% for validating. And the test data for SR were 15 images chosen from these two data sets, as shown in Fig. 4. To be fair, the test images were not used when training D.

For training D, 128×128 image patches were randomly cropped and then blurred by anisotropic Gaussian kernel, downsampled by BIC, and finally polluted by AWGN according to (1). Among them, the anisotropic Gaussian kernel is defined by a Gaussian probability density function $N(0, \Sigma)$ with a mean value of zero and covariance matrix Σ [50]. This kind of Gaussian kernel is determined by the rotation angle θ of the eigenvectors of Σ and the scaling of the eigenvalues corresponded to the eigenvectors. In this work, the rotation angle θ was set from 0 to π, and the ranges of eigenvalues e_1 and e_1 were set for ratio 2 with [0.1, 2] and ratio 4 with [0.1, 4]. It turns to isotropic Gaussian kernel when $e_1 = e_2$. The AWGN is characterized with standard deviation σ (noise level). The noise level was set to [0, 25].

Authorized licensed use limited to: Changchun Inst of Optics Fine Mechanics & Physics. Downloaded on April 19,2021 at 02:22:52 UTC from IEEE Xplore. Restrictions apply.

This article has been accepted for inclusion in a future issue of this journal. Content is final as presented, with the exception of pagination.

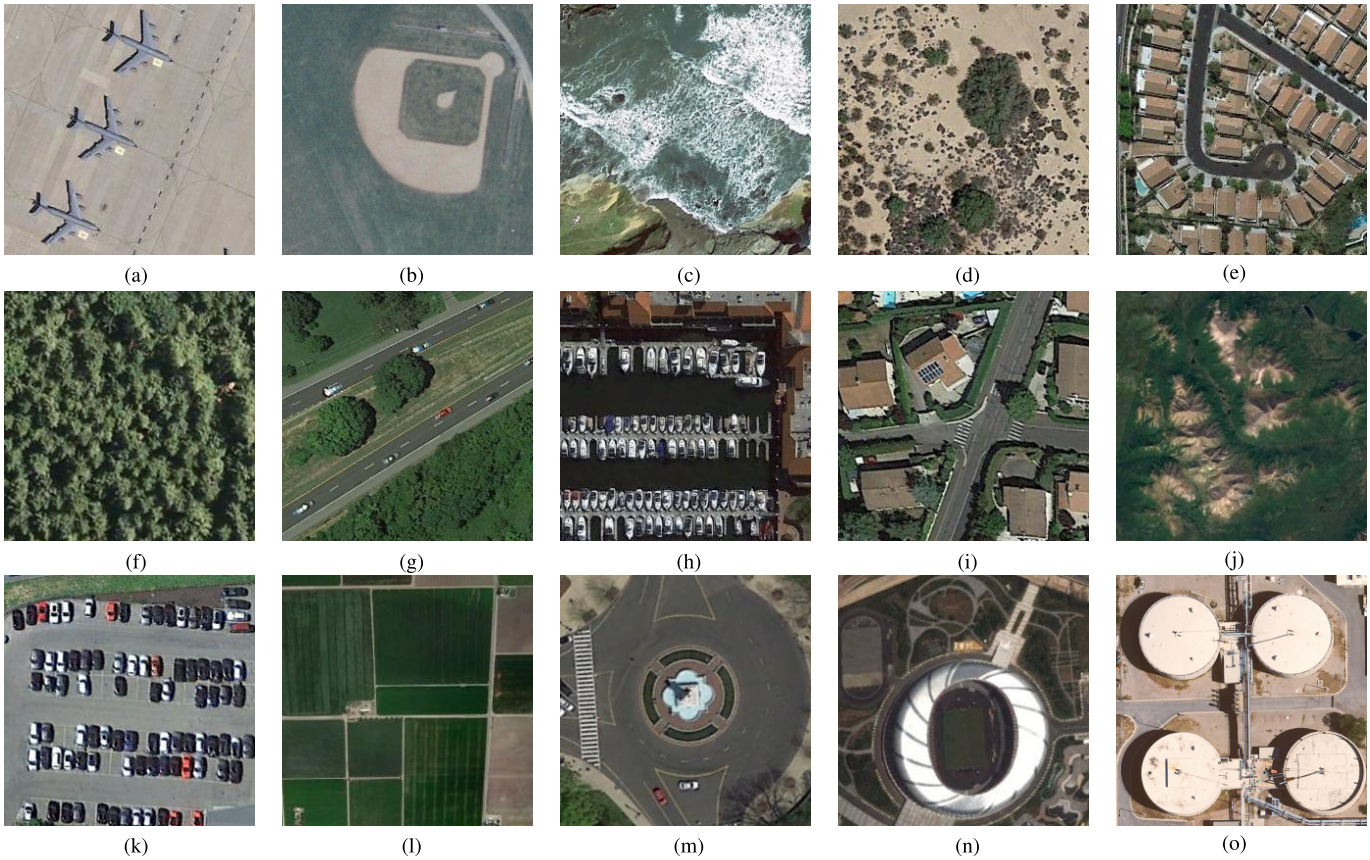

Fig. 4. Test images chosen from UCM and NWPU data sets. These images are not used during training D. (a) Airplane_645. (b) Baseballdiamond84. (c) Beach_617. (d) Chaparral_608. (e) Dense_residential_572. (f) Forest_562. (g) Freeway_621. (h) Harbor_570. (i) Intersection_561. (j) Mountain_638. (k) Parking_lot_622. (l) Rectangular_farmland_599. (m) Roundabout_651. (n) Stadium_592. (o) Storagetanks91.

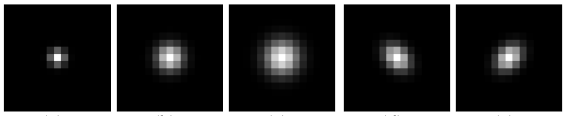

Fig. 5. Five blur kernels for multi-degradation. (a) $e_1 = e_2 = 0.5$. (b) $e_1 = e_2 = 1.5$. (c) $e_1 = e_2 = 2.5$ (only for ratio $\times 4$). (d) $e_1 = 1.8$, $e_2 = 1$, $\theta = \pi/4$. (e) $e_1 = 1$, $e_2 = 1.8$, $\theta = \pi/4$. The first three are isotropic Gaussian blur kernels, and the last two are anisotropic Gaussian blur kernels.

For reconstruction framework, we conducted experiments on 3 anisotropic Gaussian kernels and 2 isotropic Gaussian kernels as Fig. 5 shown, and noise level of 2.55 (1%) and 7.65 (3%) with kernel Fig. 5(b) to evaluate the proposed methods.

The proposed model was trained with ADAM optimizer, where $\beta_1 = 0.9$, $\beta_2 = 0.999$, and $\epsilon = 10^{-8}$. The batch size was 64 and the learning rate of D was initialized as 10^{-4}. Since the reconstruction framework is sensitive to the learning rate, we set the learning rate varying from 0.0001 to 0.01. The detailed analysis of the learning rate is presented in Section IV-D3. The whole framework was implemented in PyTorch with a GPU of NVIDIA Titan V. The code of tested methods [20]–[22], [40] and evaluation metrics were obtained from the MATLAB toolbox of SR [51].

Table I shows the evaluation metrics generally used in remote sensing image SR. Among them, root mean square error (RMSE) is presented for representing the formula of erreur relative globale adimensionnelle de synthese (ERGAS) and peak signal-to-noise ratio (PSNR). Since the tendency of RMSE is similar to PSNR, we did not use it for evaluation.

B. Results on Synthetic Images

For a comprehensive comparison, several supervised [5]–[8] and unsupervised [20]–[22], [40], [41] SR methods were chosen and evaluated both on BIC degradation and multiple degradations with ratio 2 and 4. BIC degradation is the most widely used assumption in the SR task, although it cannot effectively fit the image degradation model. Therefore, we conducted experiments on BIC degradation as a baseline; the results of BIC degradation can reflect the improvement of our method when comparing with multi-degradation.

1) Bicubic Degradation: Tables II and III present the quantitative results of evaluation on BIC degradation. The best results were highlighted with bold black and the second best results were underlined. According to Table II, our unsupervised method is superior to all the other unsupervised methods on most of the metrics. But in Table III, our method does not exceed the results of any supervised method. RCAN is the state-of-the-art method for BIC degradation and EDSR has the largest number of network parameters. Therefore, they achieve the two best results.

2) Multiple Degradations: In multiple degradations, we consider 5 blur kernels in Fig. 5 and choose one of

Authorized licensed use limited to: Changchun Inst of Optics Fine Mechanics & Physics. Downloaded on April 19,2021 at 02:22:52 UTC from IEEE Xplore. Restrictions apply.

This article has been accepted for inclusion in a future issue of this journal. Content is final as presented, with the exception of pagination.

TABLE I
METRICS FOR SR IMAGE EVALUATION

Metrics	Formula	Description
SAM	$\mathrm{SAM}(I^{SR}, I^{HR}) = \frac{1}{N}\sum_{i=1}^{N}\arccos\frac{I_i^{SR}\cdot I_i^{HR}}{\|\|I_i^{SR}\|\|\cdot\|\|I_i^{HR}\|\|}$	Spectral angle mapper is used for spectral assessment. It considers each band as a coordinate axis and computes the average angle between the pixels of I^{HR} and I^{SR}. the ideal value of SAM is 0.
RMSE	$\mathrm{RMSE}(I^{SR}, I^{HR}) = \sqrt{\frac{1}{C\cdot N}\sum_{j=1}^{C}\sum_{i=1}^{N}((I_i^{HR})_j - (I_i^{SR})_j)^2}$	Root mean square error measures the distance between the SR image I^{SR} and HR image I^{HR}, which is an error measure.
ERGAS	$\mathrm{ERGAS}(I^{SR}, I^{HR}) = \frac{100}{r}\sqrt{\frac{1}{C}\sum_{j=1}^{C}\frac{\mathrm{RMSE}((I_i^{HR})_j, (I_i^{SR})_j)}{(\bar{I}_i^{HR})_j}}$	Erreur relative globale adimensionnelle de synthese considers the ratio as a variable and measures the quality of I^{SR}. The smaller ERGAS index value means less distortion.
CC	$\mathrm{CC}(I^{SR}, I^{HR}) = \frac{\sigma_{I^{HR},I^{SR}}}{\sigma_{I^{HR}}\cdot\sigma_{I^{SR}}}$	Correlation coefficient measures the linear relationship between two images normalizing their range values. The best CC value is 1, indicating that the two images have linear correlation. In remote sensing, we typically compute the spatial correlation coefficient (sCC) over the edges detected by Canny or Sobel (this paper adopts Sobel) in images.
Q-index	$\mathrm{Q}(I^{SR}, I^{HR}) = \sum_{j=1}^{C}(\frac{\sigma_{I^{HR},I^{SR}}}{\sigma_{I^{HR}}\cdot\sigma_{I^{SR}}}\cdot\frac{2\bar{I}^{HR}\cdot\bar{I}^{SR}}{(\bar{I}^{HR})^2(\bar{I}^{SR})^2}\cdot\frac{2\sigma_{I^{HR}}\cdot\sigma_{I^{SR}}}{(\sigma_{I^{HR}})^2(\sigma_{I^{SR}})^2})_j$	Universal image Quality index evaluates three properties in the image: correlation, luminance and contrast. And larger value of Q means better quality of I^{SR}.
SSIM	$\mathrm{SSIM}(I^{SR}, I^{HR}) = \frac{(2\bar{I}^{HR}\cdot\bar{I}^{SR}+c_1)(2\sigma_{I^{HR}}\cdot\sigma_{I^{SR}}+c_2)}{((\bar{I}^{HR})^2+(\bar{I}^{SR})^2+c_1)\cdot((\sigma_{I^{HR}})^2+(\sigma_{I^{SR}})^2+c_2)}$	Structural similarity is an extension of the Q-index in order to avoid around null values. The range of its values is [-1,1].
PSNR	$\mathrm{PSNR}(I^{SR}, I^{HR}) = 20\cdot\log_{10}\frac{255}{\mathrm{RMSE}}$	A higher peak signal-to-noise ratio value represents a better image quality.

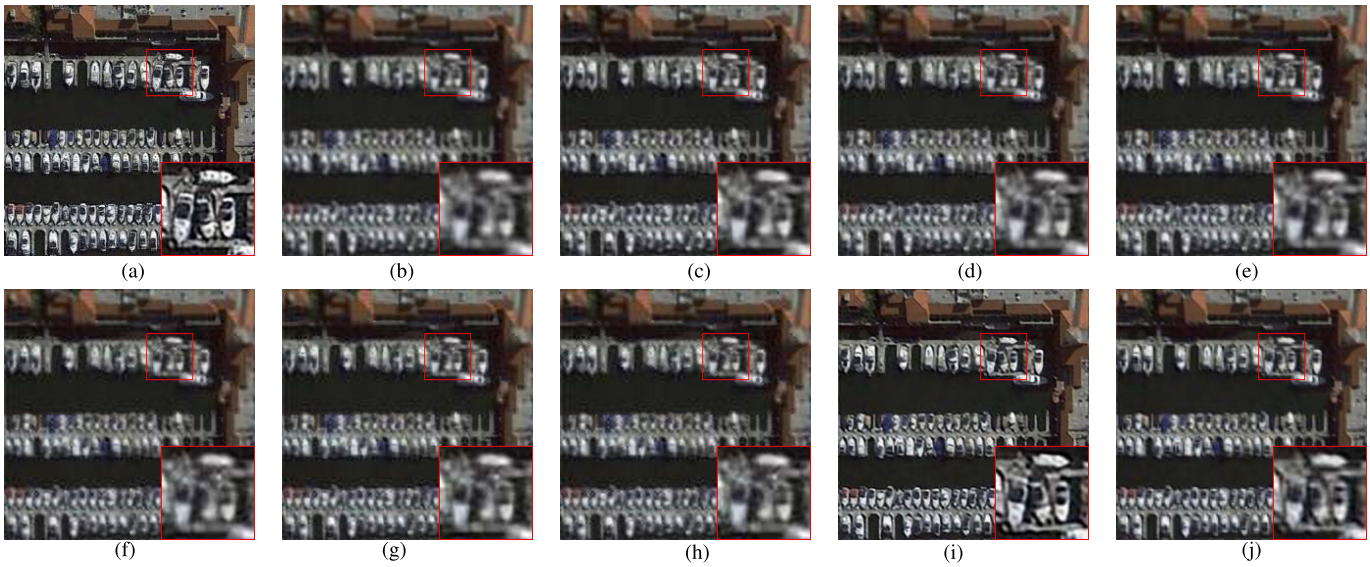

Fig. 6. Qualitative results of image "harbor_570" of several SR methods at a ratio of 2 (PSNR/SSIM), where the blur kernel is Fig. 5(d) and noise level $\sigma = 0$. (a) HR. (b) BIC (19.74dB/0.6425). (c) SRSI (20.28dB/0.6705). (d) TSE (20.27dB/0.6594). (e) ZSSR (20.20dB/0.6697). (f) EDSR (20.02dB/0.6589). (g) SRGAN (20.28dB/0.6568). (h) RCAN (20.25dB/0.6567). (i) SRMD (23.77dB/0.8693). (j) Ours (21.94dB/0.7890).

the kernels [Fig. 5(b)] to further evaluate degradation with noises. The quantitative and qualitative results are presented in Tables IV–VII, and Figs. 6 and 7, respectively.

In Table IV, compared with unsupervised SR methods, our proposed method achieved the best results on all the metrics when adopting different blur kernels. SRSI and TSE also

Authorized licensed use limited to: Changchun Inst of Optics Fine Mechanics & Physics. Downloaded on April 19,2021 at 02:22:52 UTC from IEEE Xplore. Restrictions apply.

This article has been accepted for inclusion in a future issue of this journal. Content is final as presented, with the exception of pagination.

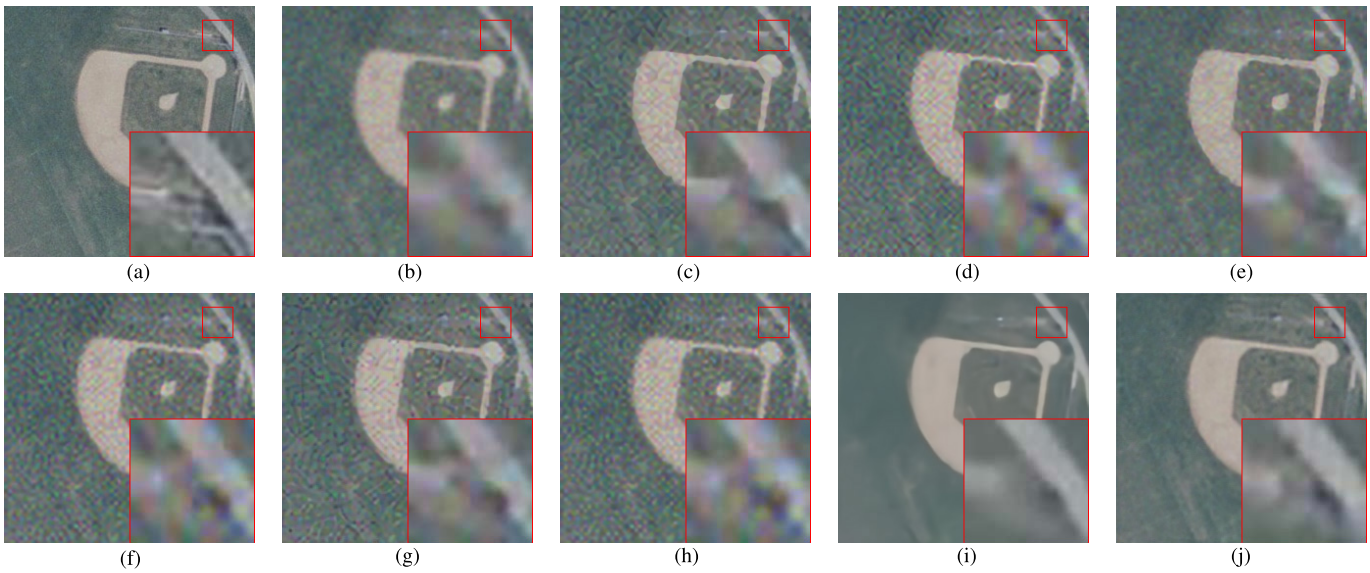

Fig. 7. Qualitative results of image "baseballdiamond84" of several SR methods at a ratio of 4 (PSNR/SSIM), where the blur kernel is Fig. 5(b) and noise level $\sigma = 7.65$. (a) HR. (b) BIC (27.68dB/0.6748). (c) SRSI (26.94dB/0.6245). (d) TSE (25.96dB/0.5208). (e) ZSSR (27.28dB/0.6637). (f) EDSR (26.32dB/0.5423). (g) SRGAN (26.09dB/0.5842). (h) RCAN (26.36dB/0.5516). (i) SRMD (30.02dB/0.7801). (j) Ours (31.36dB/0.8092).

TABLE II
AVERAGE RESULTS OF UNSUPERVISED SR METHODS ON BICUBIC DEGRADATION

Method	SAM	ERGAS	sCC	Q	PSNR	SSIM
	$\times 2/\times 4$					
BIC	0.5988/0.8229	6.9270/5.2518	0.8462/0.5877	0.8752/0.7172	26.4255/22.2723	0.7864/0.5752
SRSI [20]	0.6222/0.8681	6.5272/5.1570	0.8694/0.6175	0.8908/0.7460	27.1120/22.8587	0.8024/0.5950
LSE [21]	0.6297/0.9772	7.3385/6.9245	0.8370/0.4449	0.8778/0.6556	25.7851/19.9195	0.7906/0.5217
BDB [40]	0.6851/0.9078	10.5512/6.0866	0.6637/0.5159	0.7776/0.6909	22.7112/21.3029	0.6706/0.5230
TSE [22]	0.6226/0.8719	6.7374/5.2346	0.8569/0.6000	0.8866/0.7372	26.9140/22.8861	0.7935/0.5855
ZSSR [41]	0.6335/0.9268	6.6987/5.2103	0.8639/0.6260	0.8880/0.7346	26.8890/23.1391	0.7992/0.6161
Ours	**0.2578/0.4236**	**5.3454/4.3223**	**0.9218/0.6906**	**0.9356/0.8136**	**28.8176/24.3872**	**0.8840/0.6941**

TABLE III
AVERAGE RESULTS OF SUPERVISED SR METHODS ON BICUBIC DEGRADATION

Method	SAM	ERGAS	sCC	Q	PSNR	SSIM
	$\times 2/\times 4$					
SRCNN [4]	0.2130/0.3260	4.8120/4.1363	0.9410/0.7282	0.9484/0.8330	29.8868/24.9797	0.9017/0.7201
EDSR [5]	0.1987/0.3097	4.3619/3.7898	0.9538/0.7776	0.9563/0.8612	30.8280/25.9275	0.9154/0.7596
SRGAN [6]	0.2554/0.3668	4.8143/4.0262	0.9420/0.7458	0.9382/0.8430	29.7474/25.2402	0.8996/0.7327
RCAN [7]	**0.1899/0.3031**	**4.2396/3.7441**	**0.9565/0.7836**	**0.9591/0.8633**	**31.1366/26.0187**	**0.9213/0.7623**
SRMD [8]	0.2562/0.4010	4.6825/3.9792	0.9461/0.7549	0.9500/0.8457	30.1800/25.3530	0.9046/0.7376
Ours	0.2578/0.4236	5.3454/4.3223	0.9218/0.6906	0.9356/0.8136	28.8176/24.3872	0.8840/0.6941

render competitive results. BDB is a blind model for SR, and it is capable of handling large scale factor ($\times 4$) and more complex blur kernels. However, its results cannot surpass BIC interpolation.

According to Table V, when handling multiple degradations, SRMD rendered the best results, but our unsupervised method also obtained satisfactory results compared with other supervised methods. The first three kernels are gradually getting more blurred and the super-resolved images become worse. The last two blur kernels are spatially symmetrical and they get little difference in their results.

Fig. 6 shows the visual results of image "harbor_570" with BIC degradation and blur kernel 4 [Fig. 5(d)]. The zoomed parts showed that SRMD and our proposed method can recover the small details in the ship, but other methods cannot. Although our method did not obtain sharp edges as SRMD did, it still got a favorable result.

Then we added noises on synthetic images to test the effectiveness of the proposed method and obtained Tables VI and VII. Table VI still shows the superiority of the proposed method among other unsupervised methods. In the presence of noises, the rest of the methods achieved comparable performance. Furthermore, in contrast with Tables II and IV, the results of the proposed method show that our method can better handle multi-degradation than BIC degradation.

Authorized licensed use limited to: Changchun Inst of Optics Fine Mechanics & Physics. Downloaded on April 19,2021 at 02:22:52 UTC from IEEE Xplore. Restrictions apply.

This article has been accepted for inclusion in a future issue of this journal. Content is final as presented, with the exception of pagination.

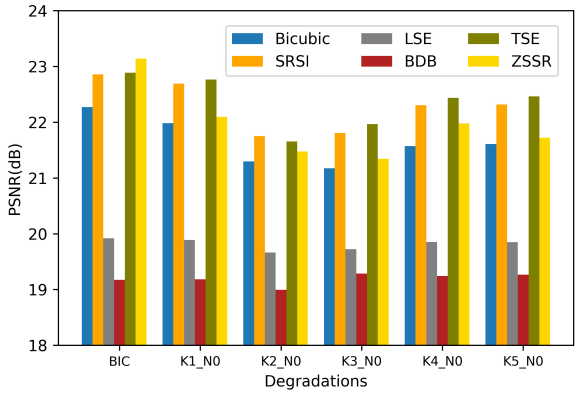

Fig. 8. PSNR results of different unsupervised methods on different blur kernels (ratio $\times 4$).

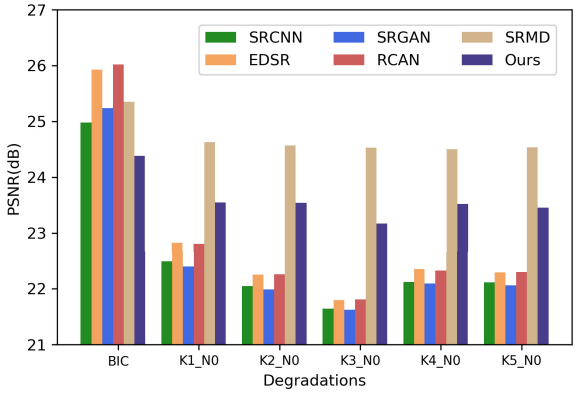

Fig. 9. PSNR results of different supervised methods and the proposed method on different blur kernels (ratio $\times 4$).

In Table VII, as noise level increases, some of the results of our proposed method can gradually exceed those of SRMD. Fig. 7 shows the qualitative results, and although the image that SRMD obtained can remove the noise, it is overly smoothed and lost some of the details. In contrast, the image of our method can remove the noise but keep the details successfully. Besides, the PSNR and structural similarity (SSIM) show the ability of the proposed method in super-resolving images with complex degradation.

3) Discussion: To evaluate the differences among different results given by different methods, we give a discussion about the above results.

First, for the hypothesis, it is reasonable to infer the results according to the experimental setup. The image only degraded by BIC degradation is of better image quality than those degraded by multiple degradations. And image quality gets poorer when involving degradations with the more blurry and higher noise level. Therefore, it can be inferred that the best SR results should be obtained by super-resolving LR images degraded by BIC. And for blur kernel and noise level, let K1–K5 mean the 5 blur kernels in Fig. 5, and N0, N2.55, N7.65 is the AWGN with noise level 0, 2.55 and 7.65. As blur and noise level increases, the SR results will be worse and worse. In addition, since RCAN is the state-of-the-art method for BIC degradation, we can infer that its results on BIC degradation are the best.

Then Figs. 8–11 give the test results in an intuitive way. Different colors mean the different methods. Although our method is an unsupervised SR method, our results are much higher than those obtained in other unsupervised methods, even comparable with supervised SR methods. So to better show the difference of results between different methods, our results are compared in supervised SR methods.

In Figs. 8 and 9, for the same method (the same color) in different degradations, except SRSI, LSE, BDB, and TSE, all the other methods get worse results as the blur increases. K4 and K5 are spatially symmetrical, and their results get little difference. And results of most SR methods based on DL are better than those without involving DL. In Figs. 10 and 11, all the methods get worse results as the noise level increases. SRMD and ours can better handle multiple degradations, but

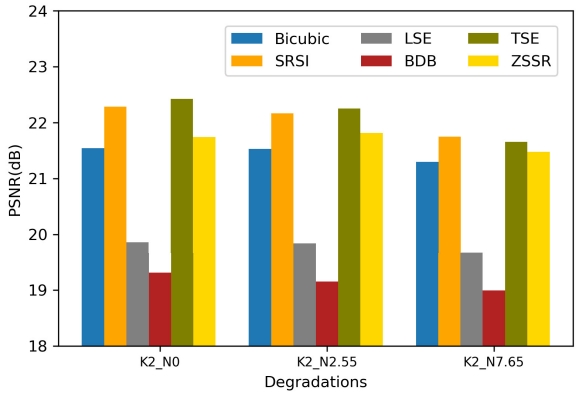

Fig. 10. PSNR results of different unsupervised methods on different noise levels (ratio $\times 4$).

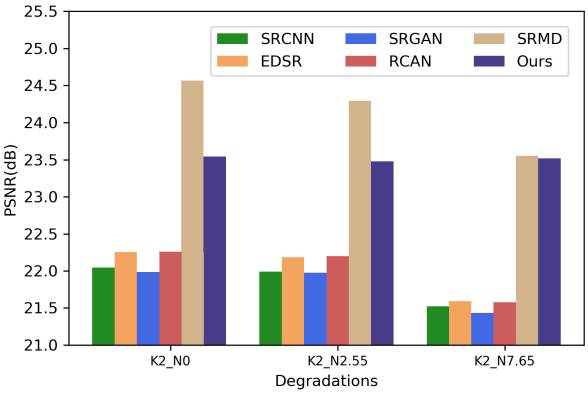

Fig. 11. PSNR results of different supervised methods and the proposed method on different noise levels (ratio $\times 4$).

other supervised SR methods achieve better results on BIC degradation; especially RCAN gets the best results, which proves the deductions above.

C. Results on Real Images

In addition to the experiments on synthetic images, we also conducted experiments on real remote sensing images. Figs. 12 and 13 are the SR results of two Jilin-1 satellite

Authorized licensed use limited to: Changchun Inst of Optics Fine Mechanics & Physics. Downloaded on April 19,2021 at 02:22:52 UTC from IEEE Xplore. Restrictions apply.

This article has been accepted for inclusion in a future issue of this journal. Content is final as presented, with the exception of pagination.

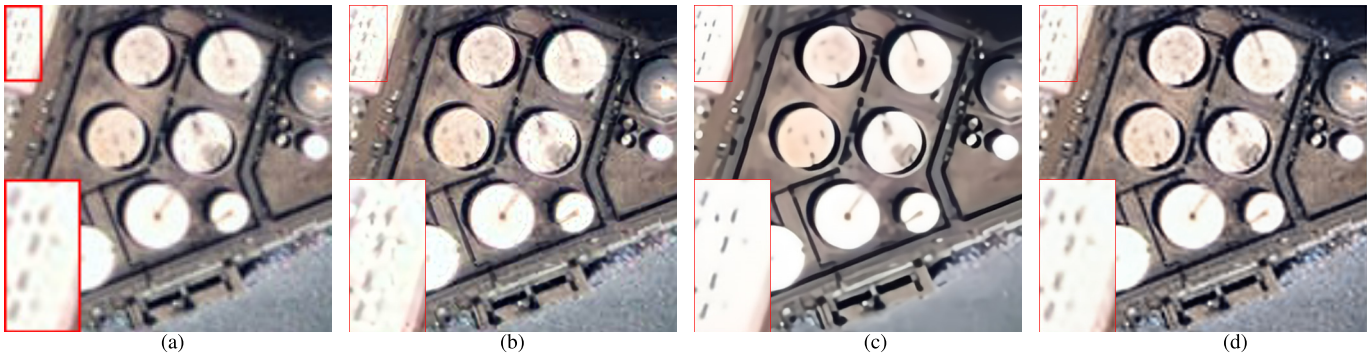

(a) (b) (c) (d)

Fig. 12. Visual results on real remote sensing image "storagetanks" obtained by Jilin-1 satellite at a ratio of 4 (NIQE). (a) LR. (b) RCAN (24.8128). (c) SRMD (25.3402). (d) Ours (23.9364).

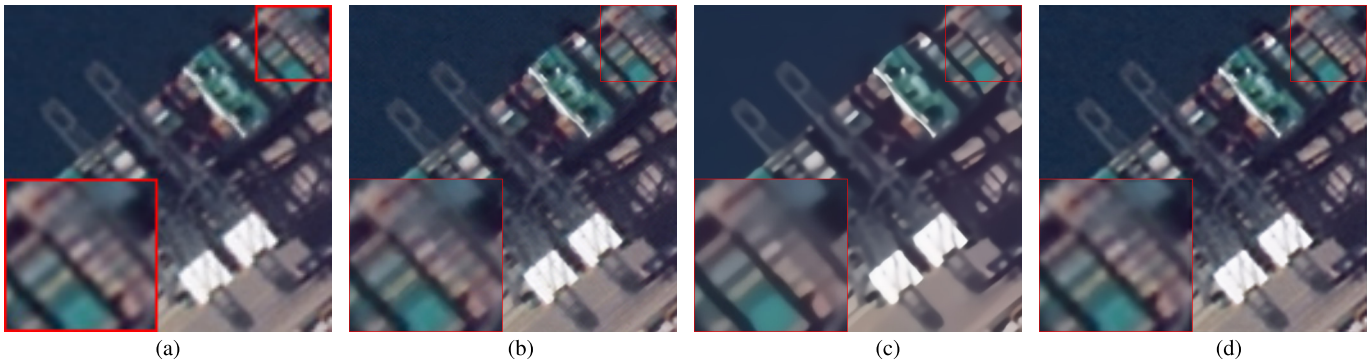

(a) (b) (c) (d)

Fig. 13. Visual results on real remote sensing image "ships" obtained by Jilin-1 satellite at a ratio of 4 (NIQE). (a) LR. (b) RCAN (34.6397). (c) SRMD (30.2989). (d) Ours (33.8438).

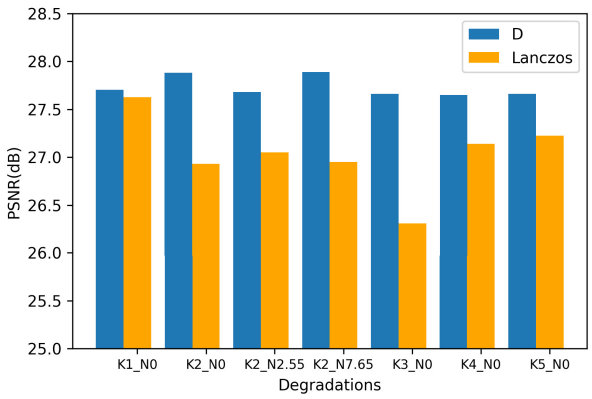

Fig. 14. PSNR results of image "stadium_592" on multiple degradations (ratio $\times 4$).

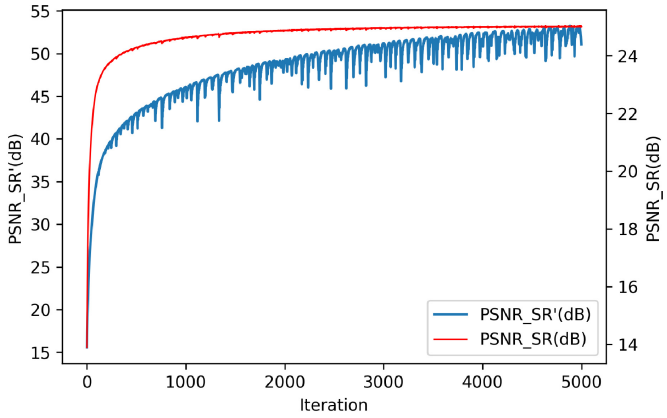

Fig. 15. PSNR curves of image "parking_lot_622" during reconstruction (ratio $\times 2$).

images. Since there is no ground truth in real images, we present visual results and use blind image quality assessment naturalness image quality evaluator (NIQE) [52] (smaller means better) for comparison. NIQE evaluates the distortion of the image. In Fig. 12, image obtained by SRMD gets the best visual result in the zoomed part and successfully handles the motion blur. But the NIQE index of the whole image is the worst, which means that it has the most severe distortions. And our result outperforms the image reconstructed by RCAN and gets the best NIQE value for the entire image. However, in Fig. 13, SRMD obtains the best NIQE but gets overly smoothed result visually. Our method can recover fine details than SRMD and get the second-best NIQE. The above numerical results and visual results on real remote sensing images demonstrate that our unsupervised SR method is very competitive and plausible in practical use compared to the state-of-the-art supervised methods.

D. Analysis of the Proposed Method

1) Ablation Study About D: Since the degrader D is one of the core modules of the proposed method, we conducted

Authorized licensed use limited to: Changchun Inst of Optics Fine Mechanics & Physics. Downloaded on April 19,2021 at 02:22:52 UTC from IEEE Xplore. Restrictions apply.

This article has been accepted for inclusion in a future issue of this journal. Content is final as presented, with the exception of pagination.

TABLE IV
AVERAGE RESULTS OF UNSUPERVISED SR METHODS ON DEGRADATIONS WITH DIFFERENT BLUR KERNELS

Method	Blur Kernel	SAM	ERGAS	sCC	Q	PSNR	SSIM
				$\times 2 / \times 4$			
BIC		0.6056/0.8210	7.6774/5.3371	0.8036/0.5767	0.8474/0.7072	25.3386/21.9830	0.7469/0.5662
SRSI [20]		0.6115/0.8552	7.0499/5.1589	0.8356/0.6100	0.8696/0.7391	26.2409/22.6930	0.7728/0.5892
LSE [21]		0.6158/0.9571	7.4930/6.8161	0.8121/0.4505	0.8626/0.6558	25.4770/19.8907	0.7667/0.5226
BDB [40]		0.6700/0.8769	10.2765/5.8710	0.6678/0.5094	0.7812/0.6898	22.8448/21.5907	0.6684/0.5330
TSE [22]		0.6053/0.8528	7.1798/5.2353	0.8289/0.5941	0.8655/0.7300	26.1340/22.7632	0.7661/0.5801
ZSSR [41]		0.6200/0.9202	7.1624/5.4869	0.8354/0.5947	0.8668/0.7197	26.0677/22.0957	0.7698/0.5836
Ours		**0.2772/0.4960**	**5.5018/4.6246**	**0.9217/0.6636**	**0.9371/0.8106**	**28.5725/23.5501**	**0.8822/0.6719**
BIC		0.6212/0.8174	8.8329/5.4984	0.7305/0.5587	0.7995/0.6867	23.8310/21.5402	0.6841/0.5496
SRSI [20]		0.6255/0.8379	8.3807/5.2569	0.7585/0.5921	0.8188/0.7206	24.4317/22.2872	0.7066/0.5734
LSE [21]		0.6262/0.9288	8.4369/6.6804	0.7473/0.4527	0.8200/0.6512	24.2298/19.8541	0.7092/0.5199
BDB [40]		0.6877/0.8636	10.7396/5.8700	0.6383/0.5063	0.7668/0.6811	22.2779/21.4767	0.6363/0.5241
TSE [22]		0.6187/0.8320	8.5269/5.3263	0.7521/0.5797	0.8128/0.7112	24.3079/22.4226	0.6992/0.5657
ZSSR [41]		0.6303/0.9132	8.5260/5.5676	0.7591/0.5780	0.8143/0.7000	24.2816/21.7438	0.7021/0.5682
Ours		**0.2850/0.4092**	**6.6494/4.6259**	**0.8709/0.6585**	**0.8951/0.8062**	**26.5409/23.5435**	**0.8194/0.6672**
BIC		-/0.8187	-/5.6419	-/0.5442	-/0.6683	-/21.1754	-/0.5353
SRSI [20]		-/0.8341	-/5.3850	-/0.5773	-/0.7023	-/21.8084	-/0.5580
LSE [21]		-/0.9147	-/6.6289	-/0.4521	-/0.6435	-/19.7263	-/0.5147
BDB [40]		-/0.8590	-/5.8841	-/0.5001	-/0.6729	-/21.4435	-/0.5169
TSE [22]		-/0.8258	-/5.4533	-/0.5670	-/0.6926	-/21.9675	-/0.5510
ZSSR [41]		-/0.8967	-/5.6607	-/0.5663	-/0.6837	-/21.3428	-/0.5531
Ours		-/**0.4071**	-/**4.7330**	-/**0.6485**	-/**0.7886**	-/**23.1703**	-/**0.6506**
BIC		0.6188/0.8163	8.7272/5.4797	0.7369/0.5608	0.8040/0.6888	23.9598/21.5743	0.6898/0.5515
SRSI [20]		0.6232/0.8378	8.2603/5.2447	0.7647/0.5944	0.8234/0.7226	24.5984/22.3041	0.7126/0.5751
LSE [21]		0.6246/0.9271	8.3409/6.6783	0.7533/0.4546	0.8238/0.6531	24.3503/19.8546	0.7145/0.5212
BDB [40]		0.6877/0.8620	10.4975/5.8597	0.6592/0.5064	0.7714/0.6822	22.9032/21.5447	0.6527/0.5255
TSE [22]		0.6163/0.8318	8.4051/5.3150	0.7588/0.5824	0.8176/0.7134	24.4403/22.4387	0.7051/0.5675
ZSSR [41]		0.6291/0.8965	8.4031/5.5331	0.7648/0.5800	0.8187/0.7047	24.3893/21.9803	0.7078/0.5709
Ours		**0.2775/0.4348**	**6.4619/4.6192**	**0.8775/0.6608**	**0.9011/0.8050**	**26.8463/23.5257**	**0.8291/0.6663**
BIC		0.6200/0.8183	8.7320/5.4852	0.7380/0.5599	0.8048/0.6885	23.9566/21.6108	0.6902/0.5509
SRSI [20]		0.6245/0.8412	8.2607/5.2503	0.7673/0.5934	0.8247/0.7222	24.5892/22.3172	0.7135/0.5748
LSE [21]		0.6247/0.9321	8.3462/6.7032	0.7550/0.4503	0.8250/0.6506	24.3868/19.8510	0.7154/0.5190
BDB [40]		0.6658/0.8658	10.4390/5.8730	0.6347/0.5046	0.7676/0.6816	22.6407/21.5544	0.6453/0.5247
TSE [22]		0.6178/0.8345	8.4073/5.3216	0.7606/0.5805	0.8186/0.7130	24.4699/22.4630	0.7060/0.5669
ZSSR [41]		0.6312/0.9130	8.4095/5.5911	0.7671/0.5761	0.8199/0.7009	24.4021/21.7214	0.7083/0.5673
Ours		**0.2781/0.4389**	**6.4707/4.6307**	**0.8791/0.6579**	**0.9027/0.8044**	**26.8583/23.4589**	**0.8306/0.6660**

(a) (b) (c) (d) (e)

Fig. 16. Visual results of image "parking_lot_622" in SR process (ratio $\times 2$). (a) Iteration 1. (b) Iteration 10. (c) Iteration 100. (d) Iteration 500. (e) Iteration 5000.

ablation experiments to evaluate its effectiveness. The proposed method has to downsample the SR image to calculate the loss function, therefore the differentiable Lanczos kernel was adopted to replace D in this framework. Fig. 14 shows the comparison of image "stadium_592" with different degradations at a ratio of 4. According to Fig. 14, a method with D can obtain better PSNR when handling the images synthesized by multiple degradations.

2) SR Process: The proposed unsupervised method is a plug-and-play method. The network parameters are gradually learned to generate SR images. For a single image, Figs. 15 and 16 show the numerical (PSNR) and visual SR process of image "parking_lot_622." In Fig. 15, PSNR_SR means the PSNR of SR image, and PSNR_SR' means the PSNR of image $I^{\mathrm{SR}'}$ degraded by I^{SR}. After about 1000 iterations, the PSNR_SR tends to be stable and increases slowly. Fig. 16 gives a visual representation. Initially, the output of G has little to do with the input. And after a few iterations, the details are gradually learned and get closer to the input image. The obtained SR image not only exploits the internal prior to approximate the input but also integrates the degradation information and external prior to images by D. Therefore, the ultimate SR image has fine details.

3) Sensitivity to the Learning Rate: As mentioned before, the proposed method is sensitive to the learning rate. In experiments, we found that the reconstruction process of some images will produce color distortion when the learning rate was small. As shown in Fig. 17, given the learning rate

Authorized licensed use limited to: Changchun Inst of Optics Fine Mechanics & Physics. Downloaded on April 19,2021 at 02:22:52 UTC from IEEE Xplore. Restrictions apply.

This article has been accepted for inclusion in a future issue of this journal. Content is final as presented, with the exception of pagination.

TABLE V

AVERAGE RESULTS OF SUPERVISED SR METHODS ON DEGRADATIONS WITH DIFFERENT BLUR KERNELS

Method	Blur Kernel	SAM	ERGAS	sCC	Q	PSNR	SSIM
		$\times 2/\times 4$					
SRCNN [4]		0.6157/0.8429	7.1769/5.1748	0.8332/0.6086	0.8665/0.7352	26.0789/22.4928	0.7684/0.5905
EDSR [5]		0.6183/0.8462	7.1730/5.1020	0.8340/0.6222	0.8659/0.7421	26.1551/22.8189	0.7673/0.5987
SRGAN [6]		0.6445/0.8564	7.3602/5.2289	0.8211/0.5942	0.8447/0.7292	25.9431/22.3986	0.7566/0.5794
RCAN [7]		0.6203/0.8493	7.2303/5.0986	0.8303/0.6214	0.8641/0.7413	26.0520/22.8028	0.7629/0.5979
SRMD [8]		**0.2407/0.3970**	**4.6884/4.2155**	**0.9472/0.7353**	**0.9508/0.8388**	**30.1413/24.6278**	**0.9051/0.7159**
Ours		0.2772/0.4960	5.5018/4.6246	0.9217/0.6636	0.9371/0.8106	28.5725/23.5501	0.8822/0.6719
SRCNN [4]		0.6283/0.8367	8.6082/5.3072	0.7517/0.5915	0.8120/0.7146	24.1232/22.0432	0.6992/0.5735
EDSR [5]		0.6312/0.8381	8.6352/5.2721	0.7493/0.5962	0.8109/0.7182	24.1673/22.2508	0.6977/0.5766
SRGAN [6]		0.6552/0.8489	8.7643/5.3556	0.7366/0.5723	0.7871/0.7083	24.1812/21.9852	0.6891/0.5614
RCAN [7]		0.6311/0.8383	8.6402/5.2726	0.7479/0.5963	0.8108/0.7170	24.1755/22.2577	0.6963/0.5759
SRMD [8]		**0.2451/0.4013**	**4.8824/4.2138**	**0.9423/0.7347**	**0.9489/0.8383**	**29.6487/24.5683**	**0.9013/0.7144**
Ours		0.2850/0.4092	6.6494/4.6259	0.8709/0.6585	0.8951/0.8062	26.5409/23.5435	0.8194/0.6672
SRCNN [4]		-/0.8339	-/5.4613	-/0.5759	-/0.6943	-/21.6405	-/0.5572
EDSR [5]		-/0.8341	-/5.4361	-/0.5787	-/0.6968	-/21.7961	-/0.5581
SRGAN [6]		-/0.8457	-/5.5019	-/0.5572	-/0.6883	-/21.6212	-/0.5446
RCAN [7]		-/0.8340	-/5.4355	-/0.5791	-/0.6959	-/21.8089	-/0.5575
SRMD [8]		-**/0.4065**	-**/4.2306**	-**/0.7327**	-**/0.8376**	-**/24.5267**	-**/0.7126**
Ours		-/0.4071	-/4.7330	-/0.6485	-/0.7886	-/23.1703	-/0.6506
SRCNN [4]		0.6265/0.8348	8.4839/5.2886	0.7587/0.5937	0.8167/0.7167	24.2674/22.1199	0.7052/0.5755
EDSR [5]		0.6295/0.8357	8.5140/5.2405	0.7557/0.6015	0.8156/0.7211	24.322722.3533	0.7036/0.5798
SRGAN [6]		0.6546/0.8472	8.6455/5.3294	0.7438/0.5772	0.7918/0.7110	24.3502/22.0950	0.6949/0.5643
RCAN [7]		0.6291/0.8362	8.5188/5.2451	0.7543/0.6013	0.8155/0.7201	24.3455/22.3237	0.7020/0.5790
SRMD [8]		**0.2485/0.3986**	**5.0384/4.2108**	**0.9355/0.7315**	**0.9443/0.8361**	**29.3727/24.5051**	**0.8946/0.7123**
Ours		0.2775/0.4348	6.4619/4.6192	0.8775/0.6608	0.9011/0.8050	26.8463/23.5257	0.8291/0.6663
SRCNN [4]		0.6273/0.8372	8.4833/5.2951	0.7606/0.5923	0.8180/0.7165	24.3208/22.1113	0.7062/0.5748
EDSR [5]		0.6301/0.8390	8.5038/5.2604	0.7598/0.5965	0.8171/0.7202	24.3535/22.2895	0.7048/0.5782
SRGAN [6]		0.6552/0.8488	8.6409/5.3462	0.7462/0.5721	0.7937/0.7100	24.3117/22.0579	0.6961/0.5627
RCAN [7]		0.6302/0.8391	8.5183/5.257	0.7567/0.5979	0.8167/0.7192	24.3645/22.3004	0.7029/0.5778
SRMD [8]		**0.2463/0.3973**	**5.0190/4.2137**	**0.9367/0.7323**	**0.9462/0.8371**	**29.4373/24.5390**	**0.8970/0.7131**
Ours		0.2781/0.4389	6.4707/4.6307	0.8791/0.6579	0.9027/0.8044	26.8583/23.4589	0.8306/0.6660

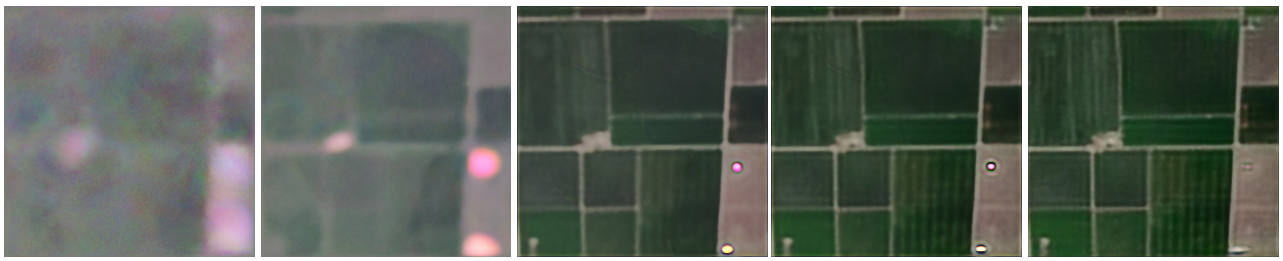

(a) (b) (c) (d) (e)

Fig. 17. Color distortion in image "rectangular_farmland_599" with learning rate 0.0001 (ratio $\times 4$). (a) Iteration 10. (b) Iteration 50. (c) Iteration 500. (d) Iteration 1000. (e) Iteration 5000.

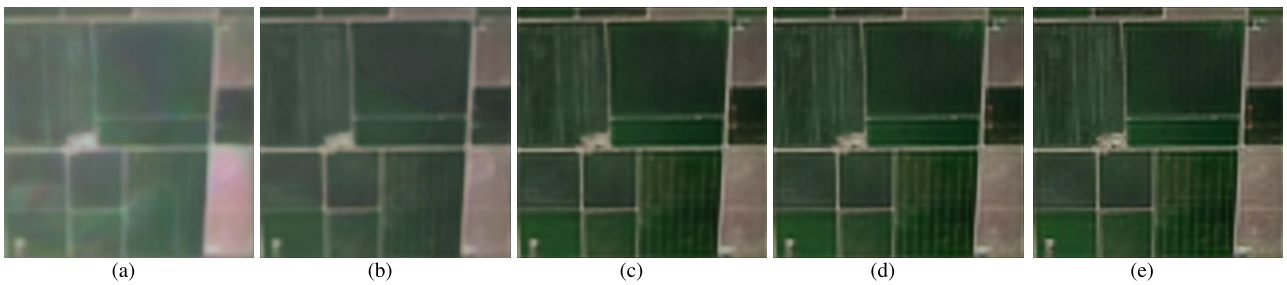

(a) (b) (c) (d) (e)

Fig. 18. No color distortion appears in image "rectangular_farmland_599" when using learning rate 0.001 (ratio $\times 4$). (a) Iteration 10. (b) Iteration 50. (c) Iteration 500. (d) Iteration 1000. (e) Iteration 5000.

0.0001, the reconstructed image did not remove the color distortion as the network iterates. But when the learning rate was set as 0.001, the color distortion will be quickly removed, as illustrated in Fig. 18. There are two possible reasons: the first one is that the small learning rate cannot meet the requirement of network parameters to capture high-level features; and another one is the limitation of the proposed method that it has to introduce image degradation to calculate loss function. In other words, after degradation, the pixels with color distortion did not present in the degraded SR

Authorized licensed use limited to: Changchun Inst of Optics Fine Mechanics & Physics. Downloaded on April 19,2021 at 02:22:52 UTC from IEEE Xplore. Restrictions apply.

This article has been accepted for inclusion in a future issue of this journal. Content is final as presented, with the exception of pagination.

TABLE VI
AVERAGE RESULTS OF UNSUPERVISED SR METHODS ON DEGRADATIONS WITH DIFFERENT NOISES

Method	Noise Level	SAM	ERGAS	sCC	Q	PSNR	SSIM
				$\times 2 / \times 4$			
BIC	$\sigma = 0$	0.6212/0.8174	8.8329/5.4984	0.7305/0.5587	0.7995/0.6867	23.8310/21.5402	0.6841/0.5496
SRSI [20]		0.6255/0.8379	8.3807/5.2569	0.7585/0.5921	0.8188/0.7206	24.4317/22.2872	0.7066/0.5734
LSE [21]		0.6262/0.9288	8.4369/6.6804	0.7473/0.4527	0.8200/0.6512	24.2298/19.8541	0.7092/0.5199
BDB [40]		0.6877/0.8636	10.7396/5.8700	0.6383/0.5063	0.7668/0.6811	22.2779/21.4767	0.6363/0.5241
TSE [22]		0.6187/0.8320	8.5269/5.3263	0.7521/0.5797	0.8128/0.7112	24.3079/22.4226	0.6992/0.5657
ZSSR [41]		0.6303/0.9132	8.5260/5.5676	0.7591/0.5780	0.8143/0.7000	24.2816/21.7438	0.7021/0.5682
Ours		**0.2850/0.4092**	**6.6494/4.6259**	**0.8709/0.6585**	**0.8951/0.8062**	**26.5409/23.5435**	**0.8194/0.6672**
BIC	$\sigma = 2.55$	0.6407/0.8379	8.8511/5.5122	0.7283/0.5565	0.7966/0.6832	23.7845/21.5327	0.6798/0.5464
SRSI [20]		0.6454/0.8586	8.4132/5.2876	0.7549/0.5871	0.8140/0.7149	24.3639/22.1661	0.6996/0.5671
LSE [21]		0.6461/0.9482	8.4722/6.6992	0.7449/0.4526	0.8150/0.6468	24.1933/19.8331	0.7024/0.5147
BDB [40]		0.6867/0.8840	10.4310/5.8997	0.6325/0.5020	0.7610/0.6750	22.7216/21.4171	0.6360/0.5168
TSE [22]		0.6546/0.8711	8.5734/5.3584	0.7460/0.5743	0.8058/0.7037	24.1866/22.2545	0.6882/0.5566
ZSSR [41]		0.6543/0.9498	8.5567/5.5895	0.7543/0.5756	0.8094/0.6972	24.1662/21.8161	0.6949/0.5625
Ours		**0.2929/0.4192**	**6.7147/4.6451**	**0.8673/0.6582**	**0.8888/0.8028**	**26.4449/23.4764**	**0.8105/0.6625**
BIC	$\sigma = 7.65$	0.7306/0.9046	9.0772/5.5743	0.7068/0.5474	0.7730/0.6597	23.4257/21.2964	0.6444/0.5221
SRSI [20]		0.7393/0.9279	8.7769/5.4505	0.7215/0.5686	0.7824/0.6834	23.8265/21.7506	0.6473/0.5265
LSE [21]		0.7363/1.0097	8.8125/6.7622	0.7182/0.4409	0.7830/0.6169	23.7059/19.6663	0.6503/0.4785
BDB [40]		0.7815/0.9770	10.7223/6.1037	0.6151/0.4821	0.7240/0.6446	22.4042/21.0562	0.5749/0.4790
TSE [22]		0.7889/0.9805	9.0219/5.5509	0.7010/0.5479	0.7684/0.6686	23.5747/21.6562	0.6240/0.5089
ZSSR [41]		0.7706/1.0067	8.9435/5.7576	0.7176/0.5592	0.7761/0.6758	23.6388/21.4782	0.6398/0.5388
Ours		**0.3032/0.4256**	**6.7441/4.6354**	**0.8648/0.6594**	**0.8857/0.8008**	**26.3303/23.5198**	**0.8045/0.6584**

TABLE VII
AVERAGE RESULTS OF SUPERVISED SR METHODS ON DEGRADATIONS WITH DIFFERENT NOISES

Method	Noise Level	SAM	ERGAS	sCC	Q	PSNR	SSIM
				$\times 2 / \times 4$			
SRCNN [4]	$\sigma = 0$	0.6157/0.8429	7.1769/5.1748	0.8332/0.6086	0.8665/0.7352	26.0789/22.4928	0.7684/0.5905
EDSR [5]		0.6183/0.8462	7.1730/5.1020	0.8340/0.6222	0.8659/0.7421	26.1551/22.8189	0.7673/0.5987
SRGAN [6]		0.6445/0.8564	7.3602/5.2289	0.8211/0.5942	0.8447/0.7292	25.9431/22.3986	0.7566/0.5794
RCAN [7]		0.6203/0.8493	7.2303/5.0986	0.8303/0.6214	0.8641/0.7413	26.0520/22.8028	0.7629/0.5979
SRMD [8]		**0.2407/0.3970**	**4.6884/4.2155**	**0.9472/0.7353**	**0.9508/0.8388**	**30.1413/24.6278**	**0.9051/0.7159**
Ours		0.2772/0.4960	5.5018/4.6246	0.9217/0.6636	0.9371/0.8106	28.5725/23.5501	0.8822/0.6719
SRCNN [4]	$\sigma = 2.55$	0.6520/0.8608	8.6381/5.3325	0.7479/0.5875	0.8073/0.7088	24.0628/21.9896	0.6918/0.5674
EDSR [5]		0.6667/0.8672	8.6748/5.3047	0.7446/0.5914	0.8046/0.7115	24.0543/22.1845	0.6873/0.5686
SRGAN [6]		0.6820/0.8705	8.8081/5.3829	0.7319/0.5676	0.7788/0.7012	24.0494/21.9722	0.6777/0.5531
RCAN [7]		0.6667/0.8660	8.6827/5.3010	0.7424/0.5926	0.8041/0.7108	24.0651/22.1983	0.6855/0.5683
SRMD [8]		0.3627/0.5149	**5.6563/4.3146**	**0.9078/0.7237**	**0.9126/0.8136**	**28.2053/24.2937**	**0.8469/0.6954**
Ours		**0.2929/0.4192**	6.7147/4.6451	0.8673/0.6582	0.8888/0.8028	26.4449/23.4764	0.8105/0.6625
SRCNN [4]	$\sigma = 7.65$	0.7597/0.9725	9.0125/5.5439	0.7106/0.5648	0.7743/0.6816	23.5450/21.5202	0.6373/0.5321
EDSR [5]		0.8110/1.0029	9.1293/5.5474	0.6999/0.5639	0.7668/0.6808	23.4999/21.5888	0.6224/0.5255
SRGAN [6]		0.8222/0.9731	9.3135/5.6162	0.6840/0.5438	0.7426/0.6729	23.3534/21.4345	0.6110/0.5154
RCAN [7]		0.8118/0.9988	9.1670/5.5355	0.6942/0.5653	0.7649/0.6807	23.4651/21.5746	0.6182/0.5261
SRMD [8]		0.5175/0.6360	**6.7128/4.6339**	0.8560/**0.6878**	0.8662/0.7615	**26.6336/23.5526**	0.7843/0.6529
Ours		**0.3032/0.4256**	6.7441/4.6354	**0.8648**/0.6594	**0.8857/0.8008**	26.3303/23.5198	**0.8045/0.6584**

image $I^{SR'}$ and cannot be removed by LR image label. However, this color distortion does not happen in every image. We found that this phenomenon occurs when there are large areas with the same color or areas with contrasting colors in images. But a large learning rate will affect the quality of SR image, leading to a decline of the evaluation metrics, such as PSNR and SSIM. Therefore, we set the learning rate between 0.0001 and 0.01 according to the diversity of input images, and when the learning rate is larger than 0.0001, it will be adjusted to 0.0001 after a certain number of iterations.

V. CONCLUSION

In this article, an unsupervised remote sensing image SR method aided by multi-degradation is proposed. In this method, the degrader D fits the image degradation model by a DNN, which can obtain images degraded by multiple degradations. Then, generator G takes an interpolated LR image as input to reconstruct SR images, together with D, forming an unsupervised SR framework. Experimental results demonstrate that the proposed method can not only achieve the state-of-the-art results compared with current unsupervised SR methods, but also render competitive results in contrast with supervised SR methods in terms of several evaluation indexes. Besides, the SR results on real images show that our method can obtain favorable images, which proves the practicality in real applications. However, this method also could be improved. For example, it is too sensitive to the learning rate and the learning rate needs to be artificially settled; as the scale factor increases, the computation complexity of inputting interpolated images is also increased and

Authorized licensed use limited to: Changchun Inst of Optics Fine Mechanics & Physics. Downloaded on April 19,2021 at 02:22:52 UTC from IEEE Xplore. Restrictions apply.

This article has been accepted for inclusion in a future issue of this journal. Content is final as presented, with the exception of pagination.

some jagged edges show up. These could be future research directions to improve the proposed method. To summarize, the proposed method provides a feasible way to reconstruct images in an unsupervised perspective and has promising potential in practical use.

REFERENCES

[1] X. Yang and Y. Yu, "Estimating soil salinity under various moisture conditions: An experimental study," *IEEE Trans. Geosci. Remote Sens.*, vol. 55, no. 5, pp. 2525–2533, May 2017.

[2] Z. Deng, H. Sun, S. Zhou, J. Zhao, L. Lei, and H. Zou, "Multi-scale object detection in remote sensing imagery with convolutional neural networks," *ISPRS J. Photogramm. Remote Sens.*, vol. 145, pp. 3–22, Nov. 2018.

[3] N. Yokoya, J. Chan, and K. Segl, "Potential of resolution-enhanced hyperspectral data for mineral mapping using simulated EnMAP and Sentinel-2 images," *Remote Sens.*, vol. 8, no. 3, p. 172, Feb. 2016.

[4] C. Dong, C. C. Loy, K. He, and X. Tang, "Image super-resolution using deep convolutional networks," *IEEE Trans. Pattern Anal. Mach. Intell.*, vol. 38, no. 2, pp. 295–307, Feb. 2016.

[5] B. Lim, S. Son, H. Kim, S. Nah, and K. M. Lee, "Enhanced deep residual networks for single image super-resolution," in *Proc. IEEE Conf. Comput. Vis. Pattern Recognit. Workshops (CVPRW)*, Jul. 2017, pp. 136–144.

[6] C. Ledig *et al.*, "Photo-realistic single image super-resolution using a generative adversarial network," in *Proc. IEEE Conf. Comput. Vis. Pattern Recognit. (CVPR)*, Jul. 2017, pp. 4681–4690.

[7] Y. Zhang, K. Li, K. Li, L. Wang, B. Zhong, and Y. Fu, "Image super-resolution using very deep residual channel attention networks," in *Proc. Eur. Conf. Comput. Vis.*, 2018, pp. 294–310.

[8] K. Zhang, W. Zuo, and L. Zhang, "Learning a single convolutional super-resolution network for multiple degradations," in *Proc. IEEE/CVF Conf. Comput. Vis. Pattern Recognit.*, Jun. 2018, pp. 3262–3271.

[9] V. Lempitsky, A. Vedaldi, and D. Ulyanov, "Deep image prior," in *Proc. IEEE/CVF Conf. Comput. Vis. Pattern Recognit.*, Jun. 2018, pp. 9446–9454.

[10] K. Turkowski, "Filters for common resampling tasks," in *Graphics Gems*. San Francisco, CA, USA: Morgan Kaufmann, 1990, pp. 147–165.

[11] M. Irani and S. Peleg, "Improving resolution by image registration," *CVGIP: Graph. Models Image Process.*, vol. 53, no. 3, pp. 231–239, May 1991.

[12] Q. Shan, Z. Li, J. Jia, and C.-K. Tang, "Fast image/video upsampling," *ACM Trans. Graph.*, vol. 27, no. 5, p. 153, Dec. 2008.

[13] L. B. Lucy, "An iterative technique for the rectification of observed distributions," *Astronomical J.*, vol. 79, no. 6, pp. 745–754, 1974.

[14] N. Zhao, Q. Wei, A. Basarab, D. Kouame, and J.-Y. Tourneret, "Single image super-resolution of medical ultrasound images using a fast algorithm," in *Proc. IEEE 13th Int. Symp. Biomed. Imag. (ISBI)*, Apr. 2016, pp. 473–476.

[15] H. A. Aly and E. Dubois, "Image up-sampling using total-variation regularization with a new observation model," *IEEE Trans. Image Process.*, vol. 14, no. 10, pp. 1647–1659, Oct. 2005.

[16] R. C. Gonzalez and R. E. Woods, *Digital Image Processing*, 3rd ed. Upper Saddle River, NJ, USA: Prentice-Hall, 2007.

[17] J. Yang, J. Wright, T. S. Huang, and Y. Ma, "Image super-resolution via sparse representation," *IEEE Trans. Image Process.*, vol. 19, no. 11, pp. 2861–2873, Nov. 2010.

[18] B. Hou, K. Zhou, and L. Jiao, "Adaptive super-resolution for remote sensing images based on sparse representation with global joint dictionary model," *IEEE Trans. Geosci. Remote Sens.*, vol. 56, no. 4, pp. 2312–2327, Apr. 2018.

[19] W. Dong, L. Zhang, G. Shi, and X. Wu, "Image deblurring and super-resolution by adaptive sparse domain selection and adaptive regularization," *IEEE Trans. Image Process.*, vol. 20, no. 7, pp. 1838–1857, Jul. 2011.

[20] D. Glasner, S. Bagon, and M. Irani, "Super-resolution from a single image," in *Proc. IEEE 12th Int. Conf. Comput. Vis.*, Sep. 2009, pp. 349–356.

[21] G. Freedman and R. Fattal, "Image and video upscaling from local self-examples," *ACM Trans. Graph.*, vol. 30, no. 2, p. 12, 2011.

[22] J.-B. Huang, A. Singh, and N. Ahuja, "Single image super-resolution from transformed self-exemplars," in *Proc. IEEE Conf. Comput. Vis. Pattern Recognit. (CVPR)*, Jun. 2015, pp. 5197–5206.

[23] K. Zhang, W. Zuo, and L. Zhang, "Deep plug-and-play super-resolution for arbitrary blur kernels," in *Proc. IEEE/CVF Conf. Comput. Vis. Pattern Recognit. (CVPR)*, Jun. 2019, pp. 1671–1681.

[24] Y.-S. Xu, S.-Y. Roy Tseng, Y. Tseng, H.-K. Kuo, and Y.-M. Tsai, "Unified dynamic convolutional network for super-resolution with variational degradations," 2020, *arXiv:2004.06965*. [Online]. Available: http://arxiv.org/abs/2004.06965

[25] K. Zhang, L. Van Gool, and R. Timofte, "Deep unfolding network for image super-resolution," 2020, *arXiv:2003.10428*. [Online]. Available: http://arxiv.org/abs/2003.10428

[26] A. Ducournau and R. Fablet, "Deep learning for ocean remote sensing: An application of convolutional neural networks for super-resolution on satellite-derived SST data," in *Proc. 9th IAPR Workshop Pattern Recogniton Remote Sens. (PRRS)*, Dec. 2016, pp. 1–6.

[27] W. Ma, Z. Pan, J. Guo, and B. Lei, "Super-resolution of remote sensing images based on transferred generative adversarial network," in *Proc. IEEE Int. Geosci. Remote Sens. Symp. (IGARSS)*, Jul. 2018, pp. 1148–1151.

[28] I. Goodfellow *et al.*, "Generative adversarial networks," in *Proc. 27th Int. Conf. Neural Inf. Process. Syst.*, 2016, pp. 2672–2680.

[29] S. Lei, Z. Shi, and Z. Zou, "Super-resolution for remote sensing images via local–global combined network," *IEEE Geosci. Remote Sens. Lett.*, vol. 14, no. 8, pp. 1243–1247, Aug. 2017.

[30] Z. Pan, W. Ma, J. Guo, and B. Lei, "Super-resolution of single remote sensing image based on residual dense backprojection networks," *IEEE Trans. Geosci. Remote Sens.*, vol. 57, no. 10, pp. 7918–7933, Oct. 2019.

[31] W. Ma, Z. Pan, J. Guo, and B. Lei, "Achieving super-resolution remote sensing images via the wavelet transform combined with the recursive res-net," *IEEE Trans. Geosci. Remote Sens.*, vol. 57, no. 6, pp. 3512–3527, Jun. 2019.

[32] S. Lei, Z. Shi, and Z. Zou, "Coupled adversarial training for remote sensing image super-resolution," *IEEE Trans. Geosci. Remote Sens.*, vol. 58, no. 5, pp. 3633–3643, May 2020.

[33] A. Bordone Molini, D. Valsesia, G. Fracastoro, and E. Magli, "DeepSUM: Deep neural network for super-resolution of unregistered multitemporal images," *IEEE Trans. Geosci. Remote Sens.*, vol. 58, no. 5, pp. 3644–3656, May 2020.

[34] S. Zhang, Q. Yuan, J. Li, J. Sun, and X. Zhang, "Scene-adaptive remote sensing image super-resolution using a multiscale attention network," *IEEE Trans. Geosci. Remote Sens.*, vol. 58, no. 7, pp. 4764–4779, Jul. 2020.

[35] C. Yi, Y.-Q. Zhao, and J. C.-W. Chan, "Hyperspectral image super-resolution based on spatial and spectral correlation fusion," *IEEE Trans. Geosci. Remote Sens.*, vol. 56, no. 7, pp. 4165–4177, Jul. 2018.

[36] W. Xie, X. Jia, Y. Li, and J. Lei, "Hyperspectral image super-resolution using deep feature matrix factorization," *IEEE Trans. Geosci. Remote Sens.*, vol. 57, no. 8, pp. 6055–6067, Aug. 2019.

[37] K. Fotiadou, G. Tsagkatakis, and P. Tsakalides, "Spectral super resolution of hyperspectral images via coupled dictionary learning," *IEEE Trans. Geosci. Remote Sens.*, vol. 57, no. 5, pp. 2777–2797, May 2019.

[38] P. V. Arun, K. M. Buddhiraju, A. Porwal, and J. Chanussot, "CNN-based super-resolution of hyperspectral images," *IEEE Trans. Geosci. Remote Sens.*, vol. 58, no. 9, pp. 6106–6121, Sep. 2020.

[39] I. Goodfellow, Y. Bengio, and A. Courville, *Deep Learning*. Cambridge, MA, USA: MIT Press, 2016. [Online]. Available: http://www.deeplearningbook.org

[40] T. Michaeli and M. Irani, "Blind deblurring using internal patch recurrence," in *Proc. Eur. Conf. Comput. Vis.*, 2014, pp. 783–798.

[41] A. Shocher, N. Cohen, and M. Irani, "'Zero-shot' super-resolution using deep internal learning," in *Proc. IEEE Conf. Comput. Vis. Pattern Recognit.*, Jun. 2018, pp. 3118–3126.

[42] T. Zhao, W. Ren, C. Zhang, D. Ren, and Q. Hu, "Unsupervised degradation learning for single image super-resolution," 2018, *arXiv:1812.04240*. [Online]. Available: https://arxiv.org/abs/1812.04240

[43] Y. Yuan, S. Liu, J. Zhang, Y. Zhang, C. Dong, and L. Lin, "Unsupervised image super-resolution using Cycle-in-Cycle generative adversarial networks," in *Proc. IEEE/CVF Conf. Comput. Vis. Pattern Recognit. Workshops (CVPRW)*, Jun. 2018, pp. 701–710.

[44] J. M. Haut, R. Fernandez-Beltran, M. E. Paoletti, J. Plaza, and F. Pla, "A new deep generative network for unsupervised remote sensing single-image super-resolution," *IEEE Trans. Geosci. Remote Sens.*, vol. 56, no. 11, pp. 6792–6810, Nov. 2018.

[45] N. Zhang, Y. Wang, X. Zhang, D. Xu, and X. Wang, "An unsupervised remote sensing single-image super-resolution method based on generative adversarial network," *IEEE Access*, vol. 8, pp. 29027–29039, 2020.

Authorized licensed use limited to: Changchun Inst of Optics Fine Mechanics & Physics. Downloaded on April 19,2021 at 02:22:52 UTC from IEEE Xplore. Restrictions apply.

This article has been accepted for inclusion in a future issue of this journal. Content is final as presented, with the exception of pagination.

[46] Y. Hou and J. Zhang, "Unsupervised remote sensing image super-resolution method based on adaptive domain distance measurement network," in *Proc. 3rd Int. Conf. Adv. Electron. Mater., Comput. Softw. Eng. (AEMCSE)*, Apr. 2020, pp. 256–259.
[47] P. Wang, H. Zhang, F. Zhou, and Z. Jiang, "Unsupervised remote sensing image super-resolution using cycle CNN," in *Proc. IEEE Int. Geosci. Remote Sens. Symp. (IGARSS)*, Jul. 2019, pp. 3117–3120.
[48] Y. Yang and S. D. Newsam, "Bag-of-visual-words and spatial extensions for land-use classification," in *Proc. 18th SIGSPATIAL Int. Conf. Adv. Geographic Inf. Syst.*, 2010, pp. 270–279.
[49] G. Cheng, J. Han, and X. Lu, "Remote sensing image scene classification: Benchmark and state of the art," *Proc. IEEE*, vol. 105, no. 10, pp. 1865–1883, Oct. 2017.
[50] G. Riegler, S. Schulter, M. Ruther, and H. Bischof, "Conditioned regression models for non-blind single image super-resolution," in *Proc. IEEE Int. Conf. Comput. Vis. (ICCV)*, Dec. 2015, pp. 522–530.
[51] R. Fernandez-Beltran, P. Latorre-Carmona, and F. Pla, "Single-frame super-resolution in remote sensing: A practical overview," *Int. J. Remote Sens.*, vol. 38, no. 1, pp. 314–354, Jan. 2017.
[52] A. Mittal, R. Soundararajan, and A. C. Bovik, "Making a 'completely blind' image quality analyzer," *IEEE Signal Process. Lett.*, vol. 20, no. 3, pp. 209–212, Mar. 2013.

Ning Zhang received the bachelor's degree from Northeastern University, Qinhuangdao, China, in 2017. She is pursuing the Ph.D. degree with the Changchun Institute of Optics, Fine Mechanics and Physics, Chinese Academy of Sciences, Changchun, China.

Her research interests include remote sensing image super-resolution and deep learning.

Yongcheng Wang received the bachelor's degree from Jilin University, Changchun, China, in 2003, and the Ph.D. degree from the Chinese Academy of Sciences, Changchun, in 2010.

He is a Researcher with the Changchun Institute of Optics, Fine Mechanics and Physics, Chinese Academy of Sciences. His research interests include image engineering and space payload embedded systems.

Xin Zhang received the bachelor's degree from Northeastern University, Qinhuangdao, China, in 2016. She is pursuing the Ph.D. degree with the Changchun Institute of Optics, Fine Mechanics and Physics, Chinese Academy of Sciences, Changchun.

Her research interests include deep learning and image classification.

Dongdong Xu received the bachelor's degree from Shandong University, Jinan, China, in 2013, the master's degree from the Harbin Institute of Technology, Harbin, China, in 2015, and the Ph.D. degree from the Chinese Academy of Sciences, Changchun, China, in 2020.

He is an Assistant Researcher with the Changchun Institute of Optics, Fine Mechanics and Physics, Chinese Academy of Sciences. His research interests include deep learning, image fusion, and embedded system software development.

Xiaodong Wang received the bachelor's degree from the Changchun University of Science and Technology, Changchun, China, in 1992, and the Ph.D. degree from the Chinese Academy of Sciences, Changchun, in 2003.

He is a Researcher with the Changchun Institute of Optics, Fine Mechanics and Physics, Chinese Academy of Sciences. His research interests include imaging technology and information processing of space optical remote sensing devices.

Guangli Ben received the bachelor's and master's degrees from Harbin Engineering University, Harbin, China, in 2013 and 2016, respectively. He is pursuing the Ph.D. degree with the Changchun Institute of Optics, Fine Mechanics and Physics, Chinese Academy of Sciences, Changchun, China.

He is also a Research Assistant with the Changchun Institute of Optics, Fine Mechanics and Physics, Chinese Academy of Sciences. His research interests include digital signal processing and space payload embedded systems.

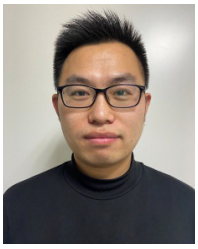

Zhikang Zhao received the bachelor's degree from the Ocean University of China, Qingdao, China, in 2019. He is pursuing the master's degree with the Changchun Institute of Optics, Fine Mechanics and Physics, Chinese Academy of Sciences, Changchun, China.

His research interests include image processing, deep learning, and remote sensing image super-resolution.

Zheng Li received the bachelor's degree from the Changchun University of Science and Technology, Changchun, China, in 2020. He is pursuing the master's degree with the Changchun Institute of Optics, Fine Mechanics and Physics, Chinese Academy of Sciences, Changchun.

His research interests cover image processing, deep learning, and object detection in remote sensing images.

Authorized licensed use limited to: Changchun Inst of Optics Fine Mechanics & Physics. Downloaded on April 19,2021 at 02:22:52 UTC from IEEE Xplore. Restrictions apply.